JOURNAL OF GEOPHYSICAL RESEARCH, VOL. 103, NO. C4, PAGES 7475–7489, APRIL 15, 1998

The variability of the tropical Atlantic

W. Cabos Narvaez and M. J. OrtizBeviá

Departamento de Física, Universidad de Alcalá, Alcalá de Henares, Madrid, Spain

J. M. Oberhuber

Deutsches Klimarechenzentrum, Hamburg, Germany

Abstract. In the present work we simulate the equatorial Atlantic variability at annual and interannual timescales using a coupled mixed layer - isopycnal ocean general circulation model (OGCM) forced with observations for the period 1980-1989. Surface features such as the seasonal variations of the equatorial system of currents or of the temperature are quite satisfactorily simulated with a relatively coarse model. For the interannual variability, the model reproduces quite well the observed warmings and coolings of the Gulf of Guinea, except for the 1981 event. The anomalies appear in the simulation earlier than in observations, and their magnitude is overestimated. These characteristics of the simulated interannual variability are shared with other simulations of the tropical Atlantic using a very different OGCM and different setup. The generation of the events is monitored through the anomalous heat content field. Although this generation can be explained in a first approximation as "the displacement to the east of warm water accumulated in the west", there are other mechanisms at work that account for the differences in the generation of the 1984 and 1988 events. Through statistical analysis the main characteristics of this field are related to other output variables and to signals in the filtered forcings. Meridional convergence in surface velocities plays a significant part in the appearance of anomalies at the Gulf of Guinea. Transition from onset stage to peak phase is connected to extraequatorial signals in the northwestern tropical Atlantic. Differences between the two simulated events (1984 and 1988) can be related to a signal in the wind forcings north of 18°N, and near the coast of Africa.

1. Introduction

The seasonal circulation in the tropical Atlantic has some traits in common with those of the other tropical oceans, such as, for instance, the equatorial system of currents or the eastern basin upwelling in summer and fall of the northern hemisphere. Other effects, such as the mainly meridional displacement of the Intertropical Convergence Zone (ITCZ), are particular to this basin. In September the ITCZ is nearer the Gulf of Mexico, in March-April it is nearest the equator and at its easternmost position. Sea surface temperatures (hereinafter SST) in the east then reach their maximum value. All the surface currents except the North Brazil Current are weak, and the zonal slope of the thermocline is almost horizontal. In May, as the ITCZ moves north, the intensification of the south trades is followed by a strengthening of the South Equatorial Current. Due to intense upwelling, the thermocline shoals in the east, a strong North Equatorial Countercurrent is observed, and measurements show that an undercurrent also exists. SST reaches its minimum value in the western part of the basin in July and a month later in the Gulf of Guinea. The countercurrent (and the undercurrent also) is very weak in winter.

The most important features of the interannual variability of the tropical Atlantic are the episodic warmings and coolings of the temperatures in the Gulf of Guinea (hereinafter GG). These are monitored by the Gulf of Guinea Index (hereinafter GGI), produced by averaging the monthly SST anomalies for the region (20°W - 10°E,3°N-12°S) [*Servain*, 1991]. The observed warming events take place every $2-4$ years, and never reach more than 1.8°K. With respect to the Pacific case, the intensity is reduced and the maxima occur more toward the center of the basin. The relationships with El Niño-Southern Oscilation (ENSO) events have been investigated in observational studies [*Wright*, 1987]. The correlation between Niño 3 and GG indices is significant, with GGI lagging, but there were Atlantic warmings not preceded by any ENSO signal. Surprisingly, precipitation in northeast Brazil is heavily correlated with the GGI, while only weakly with El Niño. Precipitation in the Sahel region is also related to the GGI. Studies of interannual variability with coupled models show systematically warming in the Atlantic as a followup of ENSO [*Latif and Barnett*, 1995].

A number of observational studies have analyzed the tropical Atlantic seasonal as well as interannual variability [*Arnault*, 1987; *Houghton*, 1991; *Weingartner and Weisberger*, 1987, 1991; *Servain*, 1991]. The seasonal cycle of the tropical Atlantic ocean has been successfully simulated by simple or general circulation ocean models [*Duchene and Frankignoul*, 1990]. Details of this circulation that are specially difficult to simulate are the object of recent studies with high-resolution models [*Johns et al.*, 1990; *Schott and Boening*, 1991].

An important drawback for the simulation of the interannual variability in this region has been the absence of a good data set of wind observations covering an extended period, the analogue of the Florida State University winds

Paper number 97JC03419.
0148-0227/98/97JC-03419$09.00

in the Pacific. Nevertheless, in the last few years there has been an increased interest in the interannual variability of the Atlantic basin, and the tropical Atlantic has received renewed attention. Some of the recent studies use coupled models, [e.g., *Latif and Barnett*, 1995], while in others an ocean general circulation models (OGCM) is forced with observations [*Carton and Huang*, 1994]. In this paper we try to understand the physical interaction determining the interannual variability of the tropical Atlantic. Some understanding of it can be gained through the statistical analysis of the available data set, as detailed in our section 2. Because these are surface data, the knowledge they provide is necessarily limited. To increase it, we will analyze a simulation of the interannual variability for the decade 1980-1989, where three warm events were observed. It was produced by forcing a mixed layer - sea ice - isopycnal ocean general circulation model with observations. Details of the model layout are given in section 3. Forcings and analysis of the simulated seasonal cycle appear in section 4. In section 5 we compare the SST anomalies of the simulated warm events with observed ones and with those of another simulation. In section 6, the onset of the events is monitored through the anomalous heat content field. Through statistical analysis, the variability of this field is reduced to two pairs of spatial patterns and their corresponding time coefficients. In section 7 these patterns of anomalous heat content are related to patterns of some variables built from the forcing fields. In section 8 we proceed to a discussion and interpretation of these results.

2. Data Analysis

While many of the features of the seasonal Atlantic variability are well documented and explained in the literature (see, for instance, *Philander and Pacanowski* [1986]), the mechanisms that determine the interannual variability and its relationships to ENSO are currently being discussed. In Figure 1 we show the GGI that is used in the present work to characterize the interannual variability of the region, from 1950 through 1982. It has been built from monthly Comprehensive Ocean-Atmosphere Data Set (COADS) SST anomalies, smoothed in time using a three-point running mean and averaged through the region marked with a box in Figure 2. All the accepted warm and cold events of *Carton and Huang* [1994] can be identified from this GGI as those with maximum values exceeding 0.6. Through simple visual inspection, three different periods can be distinguished in the record: from 1950 to 1962 events are mostly cold, from 1963 to 1979 they are warm and cold events, and from 1980 to 1992 events are mostly warm.

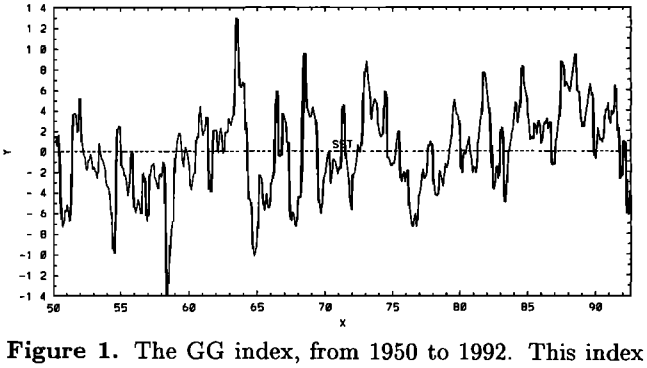

Figure 1. The GG index, from 1950 to 1992. This index was build from anomalies of SST, filtered with a three-point running mean filter and averaged to the region represented in Figure 2.

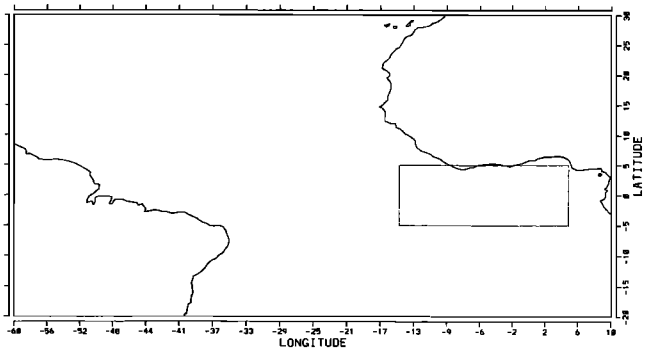

Figure 2. The box marks the location of the observations used to build the GG index.

After the climatic index, the simplest way of monitoring quasi-periodical anomalous events is through composites, built by averaging anomalies at the same stages of the evolution of the event. To build our composites we will use monthly mean of SST and wind stress observations for 1964-1992, compiled by Servain, and described by *Servain and Legler* [1986]. SST and wind data cover a band (20°S-30°N)(60°W-12°E) and are gridded in 2° × 2° boxes. Anomalies were derived in the same way as for the GGI, then filtered through a 13-month running mean, to remove the seasonal dependence. Warm composites were obtained by averaging anomalies of the same months for the events of 1972, 1981, 1984 and 1987. Cold composites were obtained from the 1964, 1967 and 1976 events. To build the composites, we make an average on the events considered, of the anomalies of each month. Composites were built for all the months of the year of the event, and all months of the year before. Because of the filter used, we cannot refer to these as winter, spring, etc., but instead refer to the different stages in the evolution of the events. The peak phase could be identified using GGI. To spot antecedent conditions, we went back from peak phase through the composites, and identified as antecedent conditions the composites appearing just before the onset of the anomalous events. The patterns represented in Figure 3 (right, top and bottom) correspond to the antecedent condition and peak phase, respectively, of the cold events. In Figure 3 (left, top and bottom) we have represented the same stages but for the warm events. The companion analysis performed on the stresses shows anomalous convergence at the equator, near the coast of Brazil, and anomalous wind stress curl, north and south of the equator, during the onset stage of the warm events and convergence at the equator in the eastern part of the basin during the peak stage. For the cold events, onset stage can be characterized by convergence north of the equator and divergence south of it, as well as by strong negative wind stress curl anomalies in the northern hemisphere. In the peak phase, there is anomalous divergence at the equator, centered around the date line.

Other interesting features of the interannual variability appear in an analysis of the covariance of SST anomalies along the line of the one performed by *Houghton and Tourre* [1992], hereinafter HT. The two empirical ortogonal func-

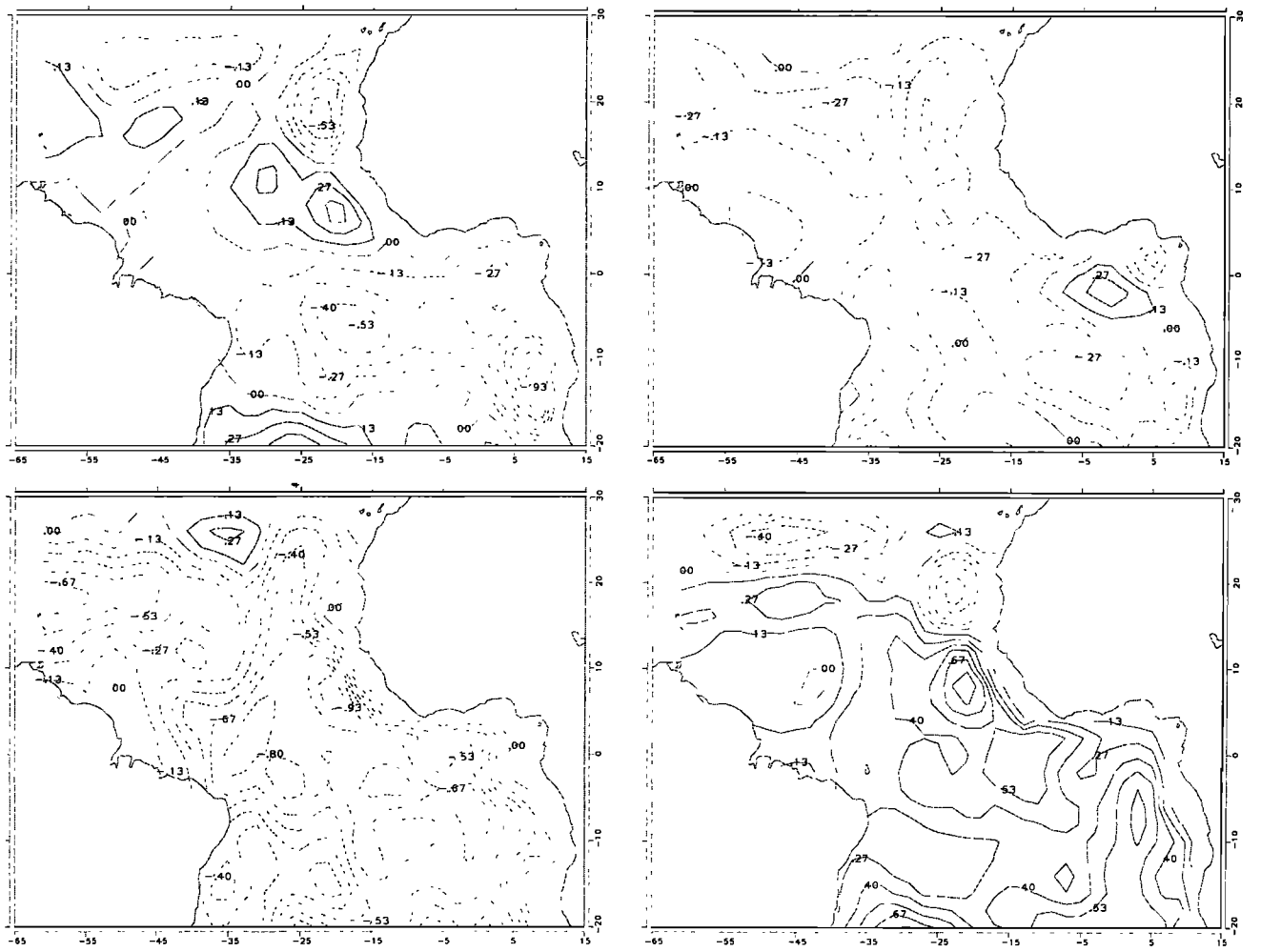

Figure 3. Composites of SST anomalies for (right) cold and (left) warm events. Top panels show antecedent conditions and botton panels show peak phase. Stages have been identified as explained in section 2.

tions (EOF), represented in Figure 4, explain 54% of the variance of the field. The first mode has a maximum at the equator, and no change of sign through the domain except for the central part of the extratropical northern hemisphere. This last trait, not present in HT analysis, is due to the inclusion of the years 1989 to 1992. The second mode, with extrema of opposite sign off the equator, is identical to HT second EOF and is known in the literature as the dipole pattern. It has been argued that while the spatial and the temporal (principal component or PC) structure of the first mode is connected with the events in the GG, the second mode and its temporal evolution represent an interhemispheric, decadal variability. Peak phase of both warm and cold events can be identified with the first mode of our analysis of the interannual variability and its reverse. As pointed out by HT the second mode cannot be identified with any situation that has been observed. Nevertheless, Figure 5 shows that a combination of both modes suffices to explain quite satisfactorily the warmings and coolings in the GG. With the solid line we represent the GGI built from the filtered (13-month running mean) anomalies of the SST field against the index obtained from a reconstruction of the field with only the two first EOFs and PCs. The PCs have been renormalized to the same variance as the GG. It seems that if the second mode represents interhemispheric variability, this kind of variability is involved in the development of the warmings and coolings of the tropical Atlantic.

3. Model Description and Layout

The model used in this work is an updated version of the model developed by *Oberhuber* [1993a]. It consists of a number of isopycnal ocean layers fully coupled to a surface bulk mixed layer model, that in turn is coupled to a sea ice model. Isopycnal models use lagrangian coordinates in the vertical, in contrast to level models, where the grid points are at fixed depth levels. The model solves full primitive equations for mass, mass flux, temperature and salinity in spherical geometry with a realistic equation of state. The layer interchange is due to diapycnal mixing and convection. A potential vorticity and enstrophy conserving scheme is implemented. In the horizontal, the equations are discretized on an Arakawa B grid. A time integration scheme consisting of a semi-implicit scheme combined with a predictor-corrector technique is used in order to achieve large time steps. The interior ocean model is coupled to the mixed layer through the entrainment-detrainment processes. The model is described by *Oberhuber* [1993a]; an updated summary can be found in the appendix. Table 1 includes the values of some of the relevant parameters adopted in the present simulation.

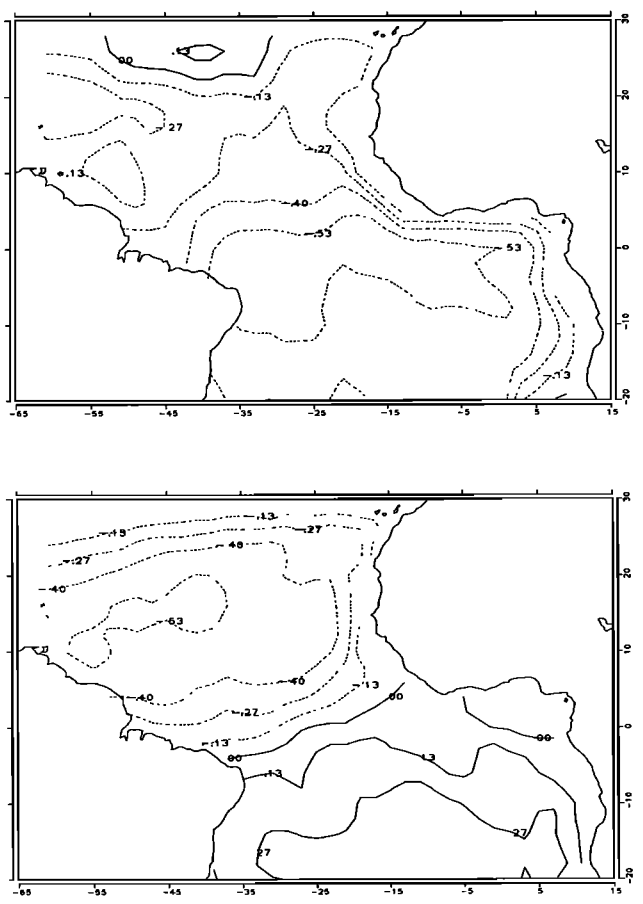

Figure 4. First and second EOF of an analysis of the SST seasonal anomalies in the tropical Atlantic, built from Servain's data set, from 1964 to 1992. The first EOF explains 41% and the second a 12% of the variance of the field.

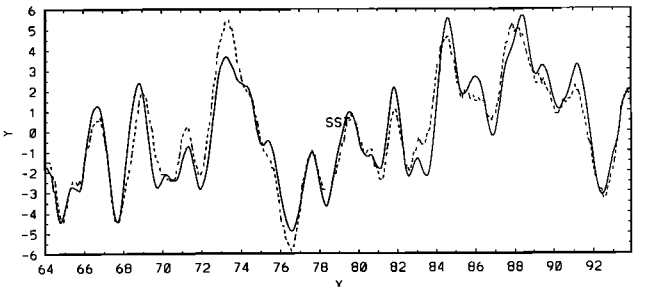

Figure 5. The solid line represents the GG index from observed SST, from which seasonal dependence has been removed through filtering. The dashed line represents the GG index computed from the field of SST anomalies reconstructed by keeping only the two first terms in the EOF expansion of the same field.

The main difference between the present version of the model and the one used in other simulations, as, for instance, *Miller et al.* [1994], consists in the way the boundary conditions in the open ocean are imposed. For the present simulation we have used a new version of the model that incorporates an open boundary formulation, due to F. Kauker and J. M. Oberhuber [*Kauker and Oberhuber*, 1997]. The main point of this formulation is that pressure is imposed only on the boundaries, while flow near the boundary is fully computed and not at all prescribed. Boundary conditions, namely the layer heights, potential temperatures and salinities, can be taken either from the observations (Levitus data set) or from the output of a global OGCM of different resolution (a simulation of the global circulation of the oceans with a version of OPYC at T106 resolution, forced with climatological winds) (Oberhuber; personal comunication).

The model domain covers 56°S to 65°N, and 80°W to 20°E. The grid varies zonally from 2.° to 1.5° and meridionally from 2.6° to 0.5°. The center of the zonal focus is in the GG, while the meridional one is at the equator. The model has 11 layers in the vertical, the time step is half a day and the model uses nonslip boundary conditions along the coasts. The domain is open to the north and south.

For the open boundary, we tried first the Levitus data set. The approach worked quite well at the northern boundary, but not at the southern. Finally, the boundary conditions are taken from the output of a simulation of the entire world ocean forced with climatological winds and fluxes derived from observations with OPYC at horizontal resolution corresponding to the grid of the T106 and the same vertical resolution. In this way, the boundary values are interpolated only horizontally, avoiding the errors introduced by interpolating in the vertical. The barotropic part of the sea level at the boundaries was estimated from the stream function of this global run using the geostrophic approximation. Nevertheless, because of the inclusion of two open boundaries, one is left with the problem of determining the differences between mean sea levels at these positions. In this case, the value of this difference in the global model can be taken only as a first indication. Then because the disparities in the global and regional model resolution are conveyed into their physics, this difference in mean sea level must be finally tuned.

Table 1. Model Parameters, Typical Values, and Description

Parameter	Typical Value	Description
c	2 m s^{-1}	reference internal gravity wave speed
m_o	0.5	coeficient for wind stirring
δt	12 hours	time step of the simulation
Ri_{crit}	0.25	critical Richardson number
h_B	20 m	penetration depth for solar radiation
κ	0.4	Karman constant
μ	1.67	constant for Ekman layer decay scale
c_T	0.0000015	surface drag coeficient

4. Simulation of the Seasonal Variability

The data sets required to force the model are air temperature, relative humidity, cloudiness, wind stress, the time-averaged absolute wind speed and its surface deviation, and surface salinity. The wind stress data are basically the climatology of the European Centre for Medium-Range Weather Forecasts (ECMWF) analysis from 1980 to 1989, corrected at the equator with the Hellermann-Rosenstein climatology [*Hellerman and Rosenstein*, 1983]. The other atmospheric forcing data required for the forcings come basically from COADS, although other global data sets were also used. The model was forced with heat fluxes Q_{obs} derived from observations according to *Oberhuber* [1988] plus a relaxation to the climatology of the observed SST:

$$Q_s = Q_{obs} - \left(\frac{dQ}{dT}\right)_{obs}(T_{obs} - T_S) \qquad (1)$$

where T_{obs} and T_S are the AMIP observed and simulated climatological SST. The relaxation coefficients $(dQ/dT)_{obs}$ are also computed following *Oberhuber* [1988]. During the last year of the spin-up, the daily values of Q_s were saved, and used afterward as the forcing in the anomalous run.

Our simulation of the seasonal cycle is satisfactory, and similar to the one reported by *Carton and Huang* [1994], and by *Huang et al.* [1995], which is noteworthy considering that the model physics and layout are very different. Their model (thereafter HCS) is basically the version by *Philander and Pacanowski* [1986] of the Cox model, based on the Geophysical Fluid Dynamics Laboratory (GFDL) model physics. The model domain covers the Atlantic from 30°S to 30°N. Its near-surface resolution is enhanced at the equator, with a grid of 1° × .5° × 10 m in the tropics that expands toward higher latitudes and 27 levels in the vertical. A nonslip condition is imposed on the coasts as well as at the artificial northern and southern boundaries, and temperature and salinity are relaxed to their monthly climatological values in their neigborhood. Horizontal mixing and diffusion are assumed constant, while the Pacanowski and Philander parameterization is adopted in the vertical. The climatological surface heating formulation includes the following features : Shortwave radiative heating between 10°S and 10°N is equal to its climatological average, decreasing linearly toward the

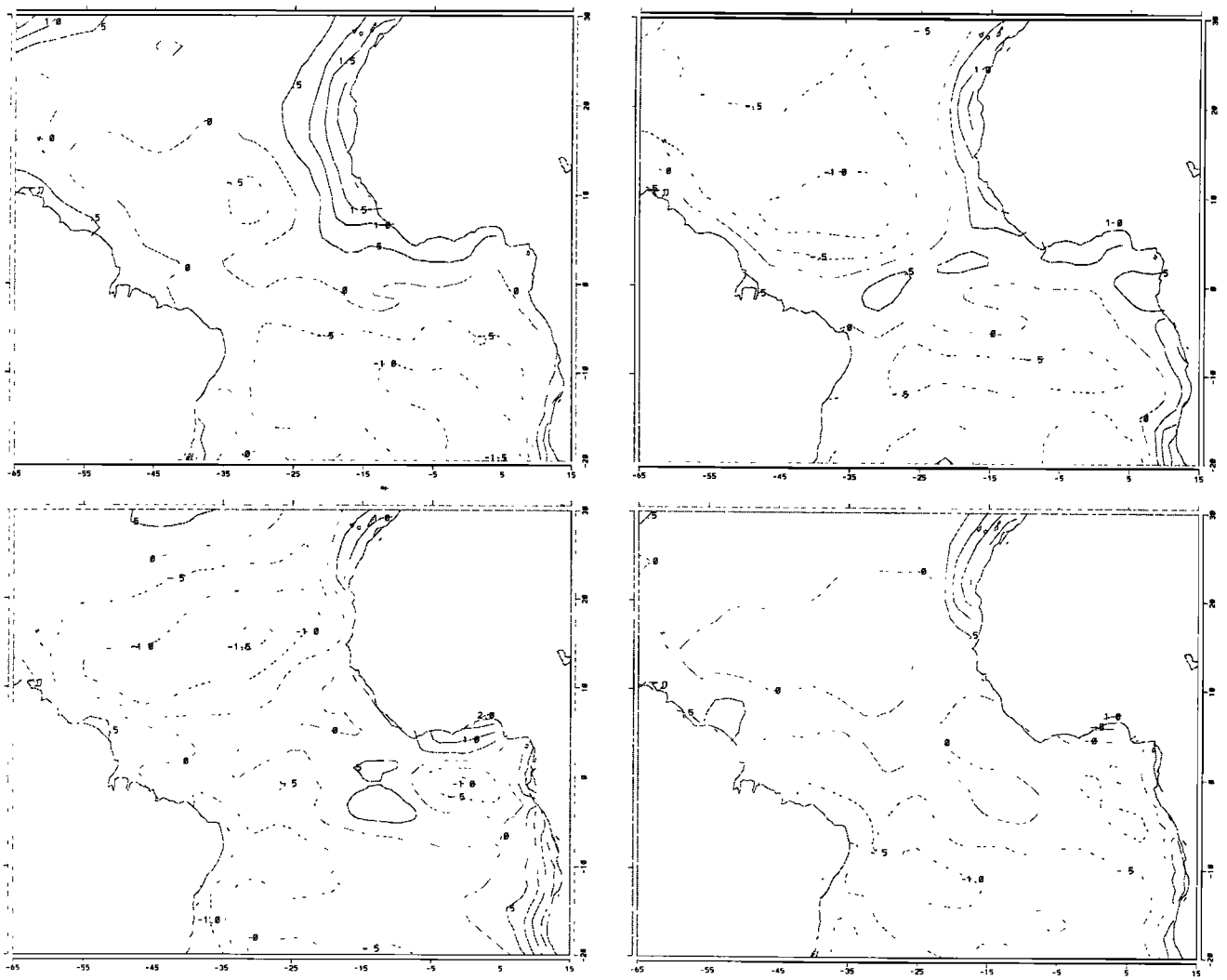

Figure 6. Monthly differences between the surface temperatures from our simulation of the seasonal cycle and the AMIP data set. The months shown are (beginning top left and going clockwise) : February, May, August and November.

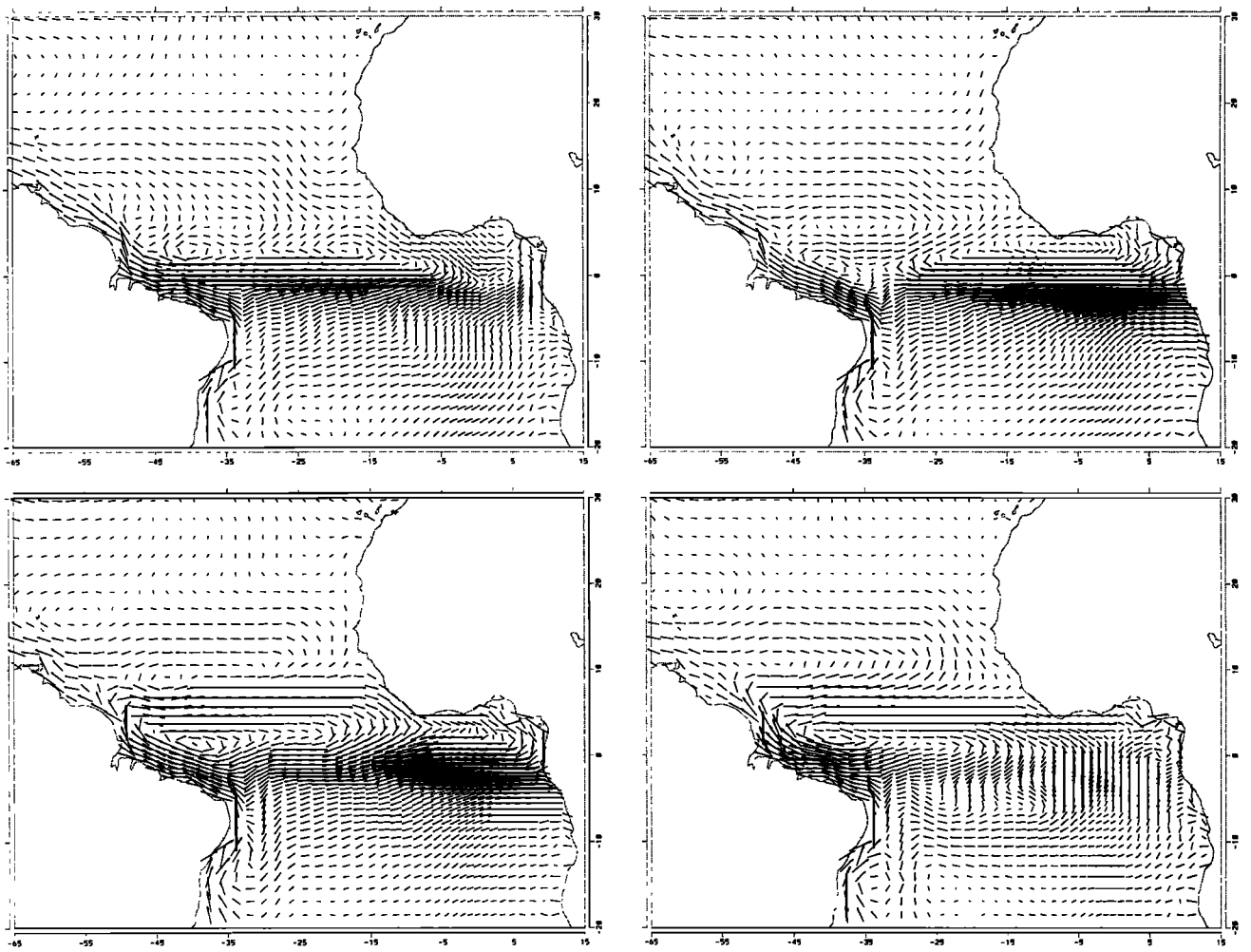

Figure 7. The mixed layer velocity of the simulation of the seasonal cycle. The months shown are (beginning top left and going clockwise) : February, May, August and November.

northward and southern boundaries. Longwave radiation is held constant over the basin, while latent and sensible heating are estimated from the air and sea temperature differences through a bulk formula. These differences are estimated from the air and sea surface temperature and from the output of the model at each grid point. The model was spun up with the climatological values of stresses derived from ECMWF-analyzed 1000 mbar winds covering the period 1980 – 1989. After this, it was integrated for the whole period using twice daily values of these stresses.

We can characterize their simulation in terms of its vertical discretization of the model (fixed levels), the physical parameterization used, the model domain and layout and the parameterization of the heat fluxes. Only the wind stresses are common to our simulation of the tropical Atlantic. In the case of the wind forcings, the differences (inclusion of a high-frequency component in their case) can be considered small. Nevertheless, both models are successful at simulating the tropical Atlantic variability at two different (annual and interannual) timescales. A comparison of both simulations may give us insight into the real phenomena.

In Figure 6, starting at the upper left panel and going clockwise, we have represented the seasonal evolution of SST errors for the annual cycle simulated with our model. The SST errors in this figure were computed by subtracting the climatological monthly mean from the AMIP (Atmospheric Models Intercomparison Project)[*Gates*, 1992] from the simulated SST. We see that even in the critical months (June-July-August) the errors are below 1°C.

In Figure 7 the seasonal evolution of the simulated currents is represented (also in clockwise sense). Some traits well captured in our simulation are the importance of the North Brazil current (hereinafter NB) together with the weak countercurrent till May and the establishment in summer of a surface equatorial gyre (formed by the South Equatorial current (hereinafter SE), a part of the NB current, the countercurrent and closed by the GG current). The weakening of the SE current in autumn is somewath too strong compared with observations. The error in the simulated magnitude of the currents is less than 20% in most of the domain [*Richardson and Reverdin*, 1987]. For the NB current, the estimated values are below 86 cm/s while observations show maximum values of 110 cm/s for some months. A feature of the observations that the model reproduces nicely is the presence of eastward currents near 13°W and between 3° and 8°S in August. Other magnitudes like mixed layer depth or the heat content have reasonable spatial structure and values.

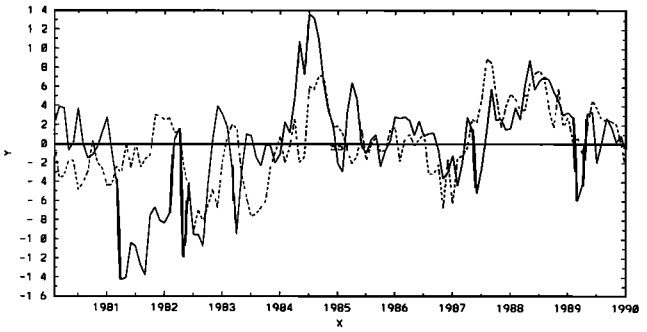

Figure 8. time evolution of the observed (solid line) and simulated (dashed line) GG index for the period 1980-89.

5. Simulation of the Interannual Variability

Using as initial state the last year of the spin-up, the model was forced with wind stress analysis from ECMWF for the period 1980-1989. The heat fluxes were obtained from the last year of the spin-up plus a relaxation to the simulated climatology given by the expression

$$Q = Q_s - \left(\frac{dQ}{dT}\right)' (T_a - T_S) \qquad (2)$$

where T_a are the SST obtained in this experiment, and T_S is the simulated SST climatology from the last year of the spinup, and $(dQ/dT)' = 0.3(dQ/dT)_{obs}$. The 0.3 is a tuning factor to obtain anomalies of the same order of magnitude as the observed ones. Anomalies of turbulent kinetic energy were not introduced in the mixed layer forcing.

In Figure 8 we show values of the Atlantic index simulated (dashed line) with our ocean model against the observed one (solid line). We see that the model captures quite well the warming events of 1984 and 1988, but the 1981 event is simulated as one of cooling. In Figure 9 the peak phase of the simulated warmings (left panels) is compared with observations (right panels). The equatorial character of the simulated warming is a trait shared with HCS, as well as the higher values of the anomalies with respect to observations. From a comparison month by month of the observed and simulated 1988 event (not shown) it can be seen that the starting of the episodes is well modeled. It is later, when the anomalies extend to the tropics along the African coasts, that the model does not perform well, although the event is ended at the right season (winter 1989).

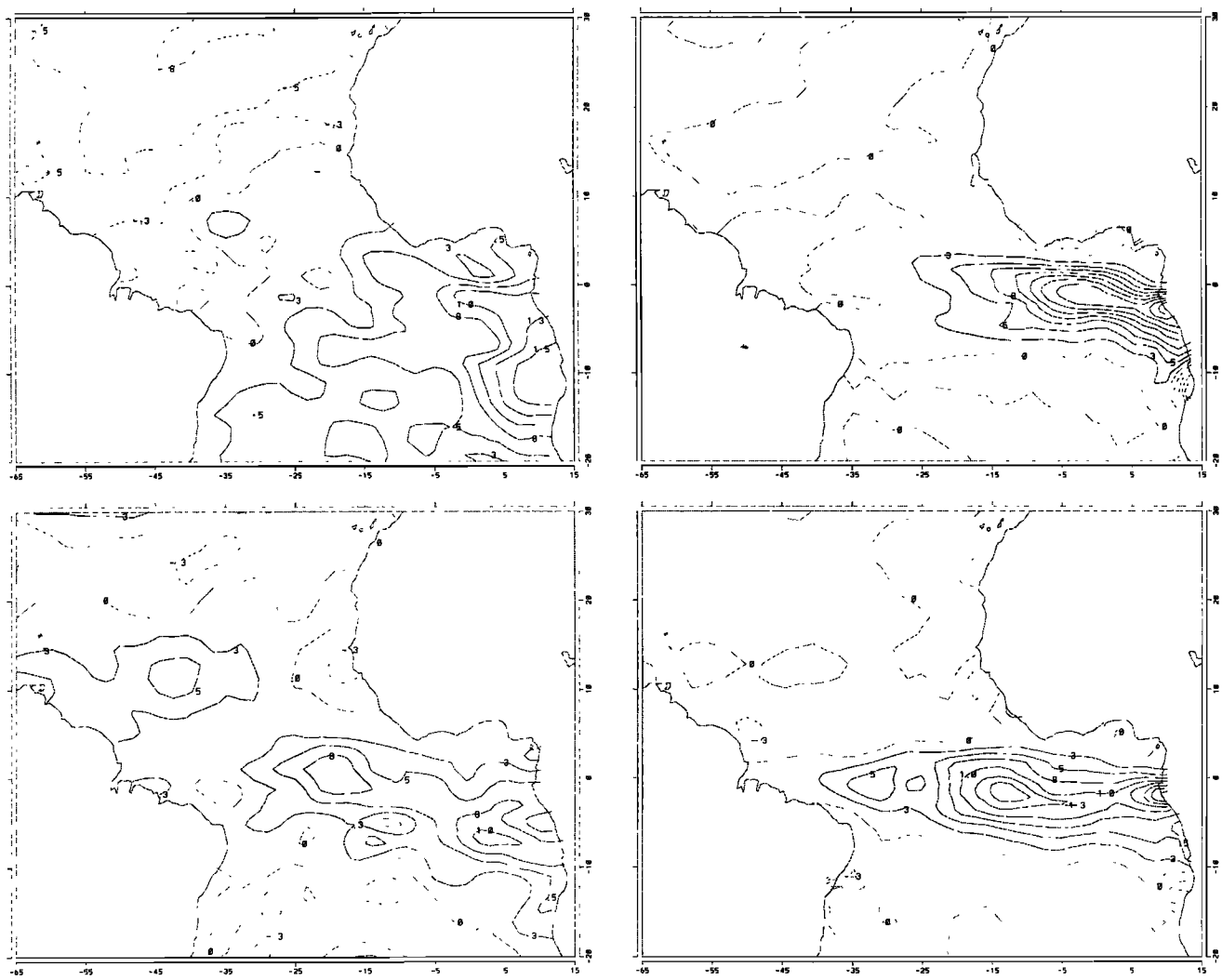

Figure 9. Peak phase of the warmings of 1984 and 1988 (right) from Servain data and (left) from our simulation.

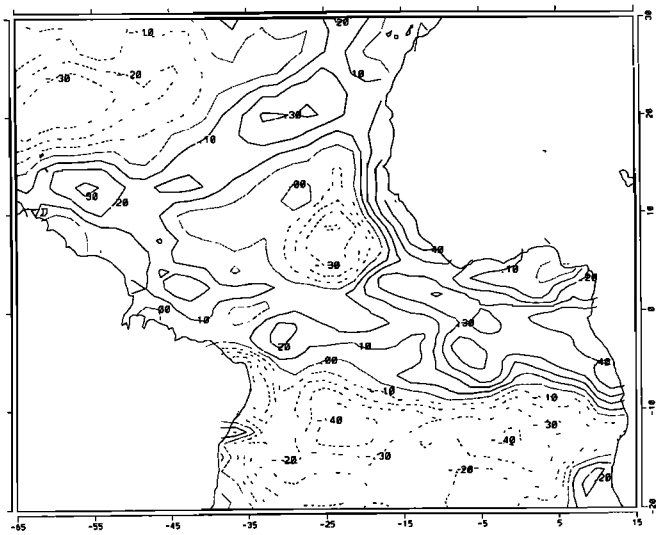

Figure 10. Correlation between observed and simulated SST anomalies.

An interesting feature, common to the HCS simulation and ours, is the misrepresentation of the 1981 event. This common trait supports HCS's conclusion that a trend in the ECMWF winds is responsible for this failure. The magnitude of the simulated SST anomalies (too big) can also have a part in this mismatch between the simulated and observed world. After this failed warming event, a brief cooling episode in the observations is well represented in our simulation (not shown). The evolution of the cooling events (observed and simulated) compares well with the reverse of the warming events (observed and simulated respectively): the modeled cooling also appears earlier than the observed one.

Some other statistical features of the simulated interannual variability can be found in Figure 10, where the correlation between observed and simulated SST anomalies is represented. To be significant, correlations must be roughly greater than 0.2. Maximum values appear at the equator and east of 8°W. The seasonal evolution shows that the correlation between observed and simulated anomalies reaches a maximum in summer, while in autumn the values are smaller and small-scale phase reversals are noticeable.

6. Onset of the Anomalous Events

A useful variable to monitor the start of the anomalous events is the heat content hc stored in the upper ocean at each horizontal grid point (x, y) and at each instant of time t as

$$hc(t,x,y) = \rho c_p \int_{h_0}^{0} (T(t,x,y,z) - T_0(t,x,y)dz \qquad (3)$$

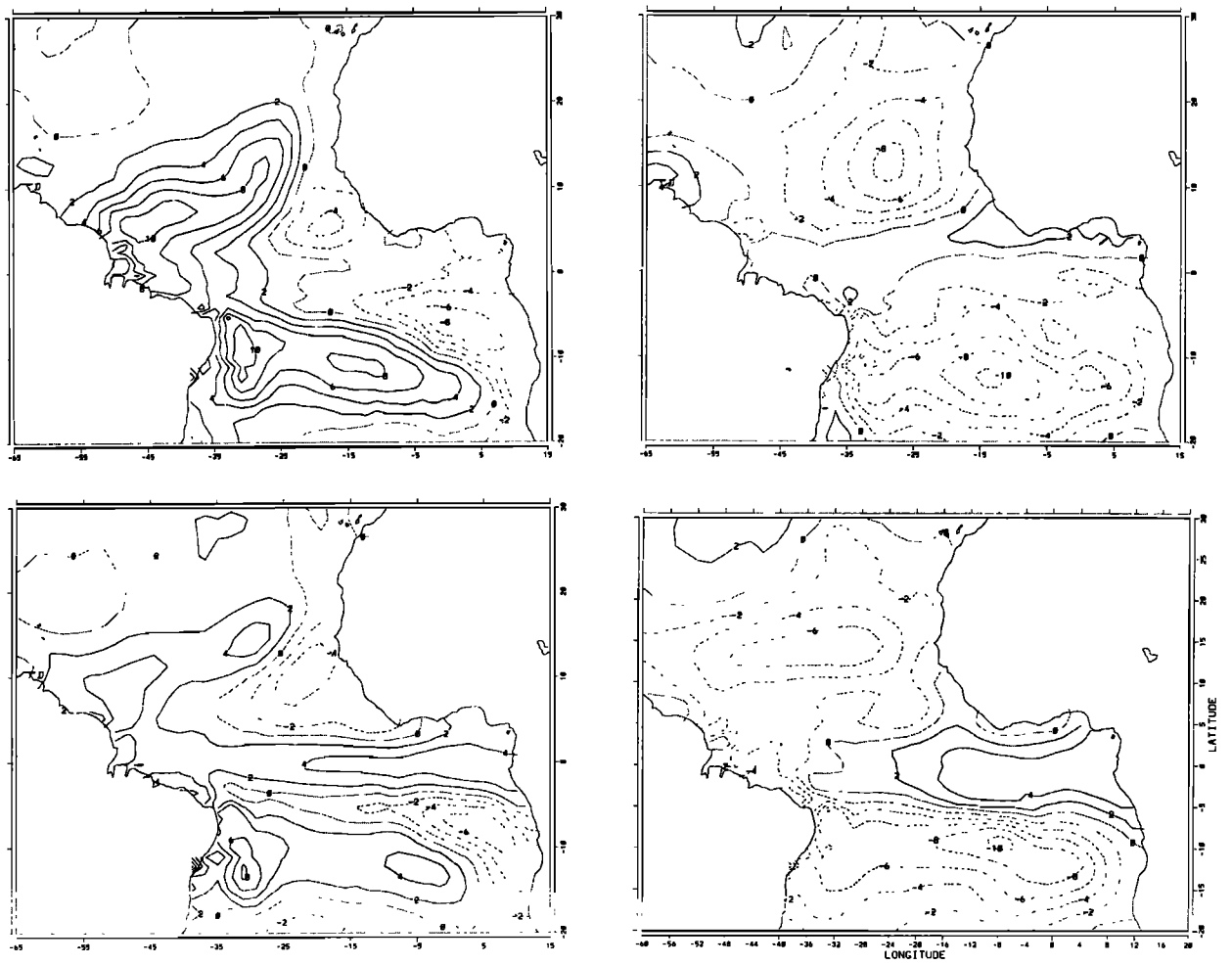

Figure 11. Antecedent conditions (top panels) and initial stage (bottom panels) of the 1984 (left panels) and the 1988 (right panels) warmings.

where $T_0(t,x,y)$ is the temperature at a reference depth $h_0 = 360$ m and the same horizontal grid point and time t. It estimates the relative thermal energy stored in the upper ocean active layer.

In the ENSO case, changes of this variable anticipate the appearence of the anomalous SST [*Chao and Philander*, 1993]. This feature is also present in our Atlantic simulation, as shown in Figure 11, where the antecedent conditions to the 1984 and 1988 warmings are presented. In the case of the 1984 event (Figure 11, left panels), antecedent conditions like the ones found for the ENSO case are clearly identifiable in the previous autumn (top left): There is a heat content accumulation in the western part of the basin, with centers north and south of the equator and a strong gradient along it. We will refer to this pattern as HC2. In the next season (winter 1984, bottom left), the heat accumulation in the eastern equator referred to by HCS as the initial stage of the events is recognizable in a pattern hereinafter referred to as HC1a. There is no equivalent to HC2 to be found in the seasons previous to the 1988 event (Figure 11, right panels). Antecedent conditions of this event can be traced back as far as the spring of the preceding year, where warm water seems to accumulate at the eastern basin, while the heat content in the tropics is anomalously low. If we compare only the equatorial region, between 8°S and 8°N, this pattern has similarities with HC1a and therefore will be called HC1b. Both antecedent conditions, HC2 and HC1b, are traceable to anomalies of the currents, both outside and at the equator, that are traceable to anomalies in HC1b, are traceable to anomalies of the currents, both outside and at the equator, that are traceable to anomalies in the wind forcings. For instance, in the autumn of 1983 there is a strengthening of the North Equatorial current (NEC) and negative anomalies in the southern gyre, while in the spring of 1987 the situation is reversed; the anomalies of the currents in those two regions are positive. In both cases there are also important disturbances along the equator.

7. Statistical Analysis of the Simulated Interannual Variability

The characteristics of the simulated interannual variability and its relationships with the annual cycle can be summarized through a statistical analysis that captures the most relevant features of this variability in both space and time. To this aim and due to the short length of the series, we use a version of the technique known as POP (principal oscillation pattern) analysis [*Storch et al.*,1993]. Propagating features

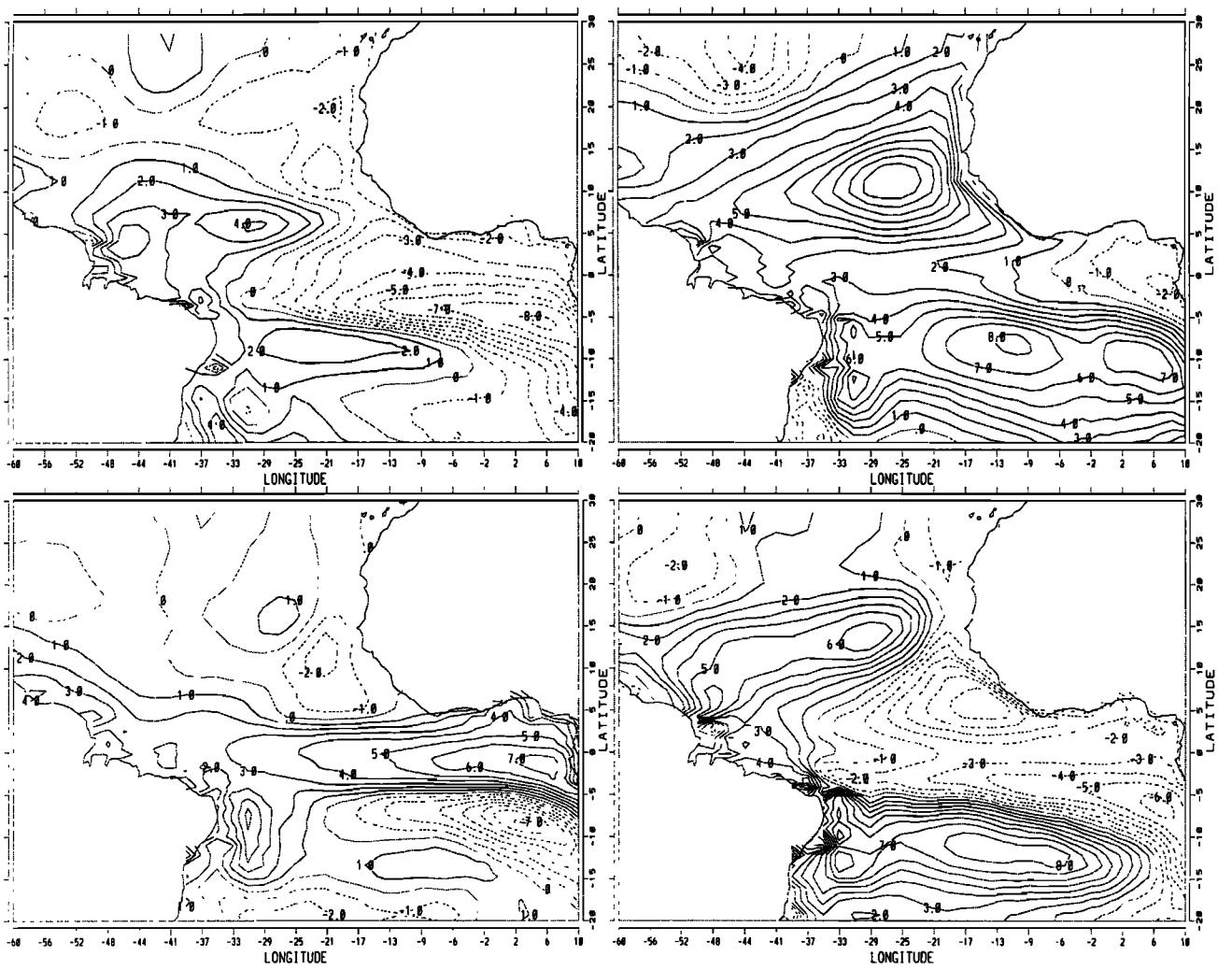

Figure 12. The pair (left) of POPs 2/1 and (right) POPs 3/4 of the seasonal anomalies of the simulated heat content anomalies.

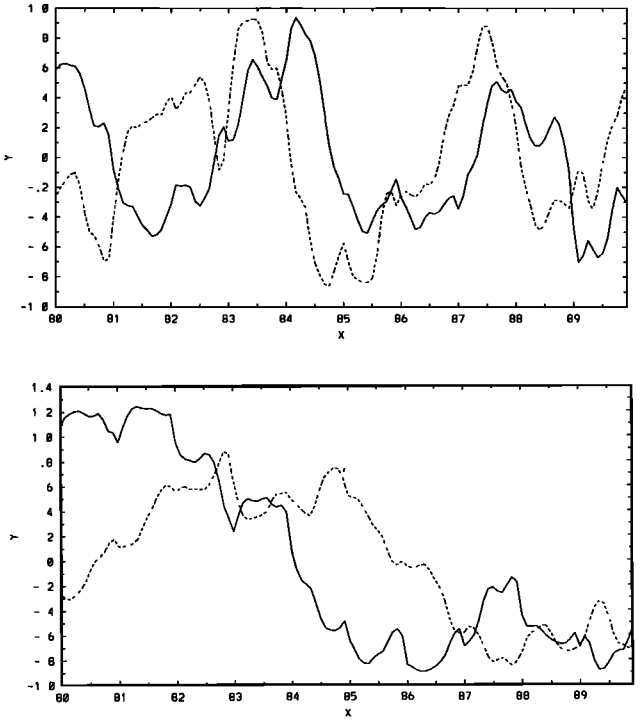

Figure 13. Empirical time coefficients of (top) the first pair of POPs (time coefficient 1, solid line; time coefficient 2, dashed line) and (bottom) the second pair of POP of the simulated heat content anomalies. (time coefficient 3, solid line; time coefficient 4, dashed line).

can be better noticed in the POP analysis of the anomalous heat content. Anomalies of this field were built by substracting the seasonal mean (the mean for each month) from the simulated value at the 15th of each month. The anomalous field was then smoothed, using a three-point running mean average. Previous to the POP analysis, we proceed to the customary reduction of the degrees of freedom of the field by an EOF expansion and further truncation. The four first EOFs retained explain 90% of the variance of the field. The patterns are presented in Figure 12 and their time evolution in Figure 13. POP 2, shown in Figure 12 (top left) is akin to the HC2 pattern discussed in section 6, while the POP 1 represented in the same figure (bottom left), corresponds to the onset stage, HC1. Their time coefficients, shown in Figure 13 (top), conform well to the POP evolution scheme : $P_2 \rightarrow P_1 \rightarrow -P_2 \rightarrow -P_1$. Maximum positive values in the time coefficient of POP 2 precede by 1 year the 1984 event, and its maximum negative values are coincident with the peak mature stage of the episode. The time coefficient of POP 1 has maximum positive value in the spring of 1984. Together, this first pair of POPs give a picture of the generation of the event in good agreement with *Wyrtki's* [1985] hypothesis. On the other hand, neither the pair of POP 3/4 nor their time coefficients give a clear picture of the evolution of the events.

It seems important at this point to remember that POPs belonging to different pairs are not orthogonal and therefore that the total variance explained by the two pairs can not be obtained simply by adding the variance explained by each pair. Therefore, the contribution of each pair to the evolution of the anomalous heat content field has to be estimated in a less straightforward way. For this, three different anomalous heat content indices are built by averaging anomalies of the heat content through the same box used for the GGI. First, the anomalous heat content field is obtained from a reconstruction of the field with only the first four EOFs (10% of the variance of the field is then lost). This reconstructed field is identical to the one obtained with all four POPs. Second, the field is reconstructed with the only the pair of POPs 3/4. Those are the indices represented in Figure 14 with the short-dashed line, solid line, and long-dashed line, respectively. We can see from them how the evolution of the heat content in the region of interest is basically accounted for by the first pair of POPs. The second pair correct this picture, introducing the differences between the 1984 and 1988 events, as has already been discussed in section 6.

The interannual variability of the tropical oceans is characterized by some indexes (El Niño 3, the GGI,etc.) built from the anomalous SST field. Nevertheless, the preceding analysis shows that the generation of the events is better understood by the statistics of the heat content field. To compute the anomalous heat content field, knowledge of the anomalous temperatures of the water column down to 360 m is required. Model output statistics can help us to relate the heat anomalies to those of other variables of the simulation (not only sea surface temperature, but also surface velocity or mixed layer depth) and/or of the forcings

To model this relationship in the simplest way, we use a multivariate lagged regression.Let $s_j(t)$ be the time coefficient of the jth POP of the heat content anomalies, and $r_k(t)$, the kth principal component of some of the other simulated fields or of the forcing fields. Then

$$s_j(t) = \sum_{k=1}^{p} a_{jk}^{l} r_k(t-l) \qquad (4)$$

where l is a fixed time lag. The value of l is allowed to vary in a range from -6 to +6 months. For a certain j, to take into account a $r_m(t)$ and a lag l, two statistical tests have to be passed. Only the a_{jm} that are significantly different from 0 will be considered and, in any case, the variance explained by the signal has to be greater than the residuals. For those regressions that passed both tests, we proceed to visual inspection.

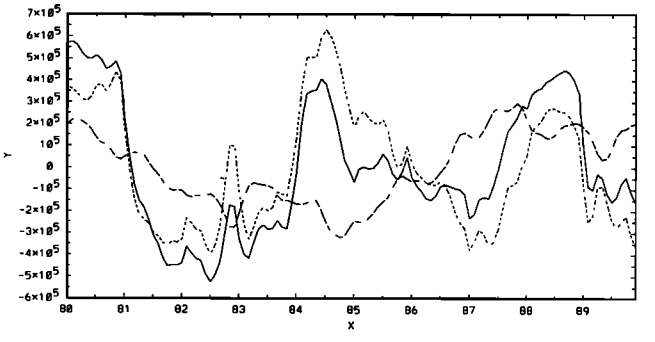

Figure 14. Short dashed line depicts an index of the GG anomalous heat content, built from a reconstruction of the field using four EOFs. Thin solid line depicts the same index but for the anomalous heat content field reconstructed with the first pair of POP. Long dashed line shows the index as built from the anomalous heat content field reconstructed with the second pair of POP.

Next, the anomalous fields of SST, mixed layer depth and mixed layer zonal and meridional velocities were expanded in terms of their EOFs. Retaining four EOFs in this expansion, we can explain 83% of the variance in the case of the SST anomalies, 62% in the mixed layer depth, and 79% in the zonal and 69% in the meridional mixed layer velocity. Then we proceed to use the four first principal components of these fields to model the time coefficients of the four first POPs of the heat content. None of the selected fields yielded a satisfactory simulation of all four time coefficients. The field that performed best was the meridional mixed layer velocity: The appearence of the warmings in the GG is due, in part, to an anomalous convergence of the meridional velocities in the mixed layer.

On the contrary, the forcing anomalies cannot be reduced to a few modes as in the case of the anomalies of the oceanic variables. Therefore, we try to define for each grid point a variable that will measure its persistence rather than the forcing. Such variable is defined as

$$\theta_w = \int_{t-t_d}^{t} wc(\vec{r}_H, t')dt' \tag{5}$$

where wc stands for the forcing variable (that is, zonal or meridional wind or equivalently the wind stress curl and its divergence), $\vec{r}_H$ locates the grid point and t_d is the characteristic decorrelation time at this point.

For the present analysis and to allow for an easier interpretation, the wind forcings were resolved in terms of wind stress divergence and its curl. For each of these variables, seasonal anomalies were computed as usual. The anomalous values of the integrated forcing variables $\theta_{\vec{\nabla}\vec{\tau}_w}$ and $\theta_{\vec{\nabla}x\vec{\tau}_w}$ were then computed using (5). We then proceed to a reduction of the number of degrees of freedom of the field through an expansion in terms of EOFs. The variability of the field is well represented in terms of its six first EOFs, explaining 71% and 61% of the variance of the anomalies of the integrated wind divergence and curl, respectively.

When the regression of the $r_m(t-l)$ at lag l gives a satisfactory simulation of the $s_j(t)$, the regression coefficients allow for the identification of a spatial structure in the forcings whose temporal evolution gives an estimation of the heat contents with a certain lag. These patterns are known as associated patterns and are given by

$$\vec{v}_j = \sum_{k=1}^{p} a_{jk}^{l} \vec{e}_k^{l} \tag{6}$$

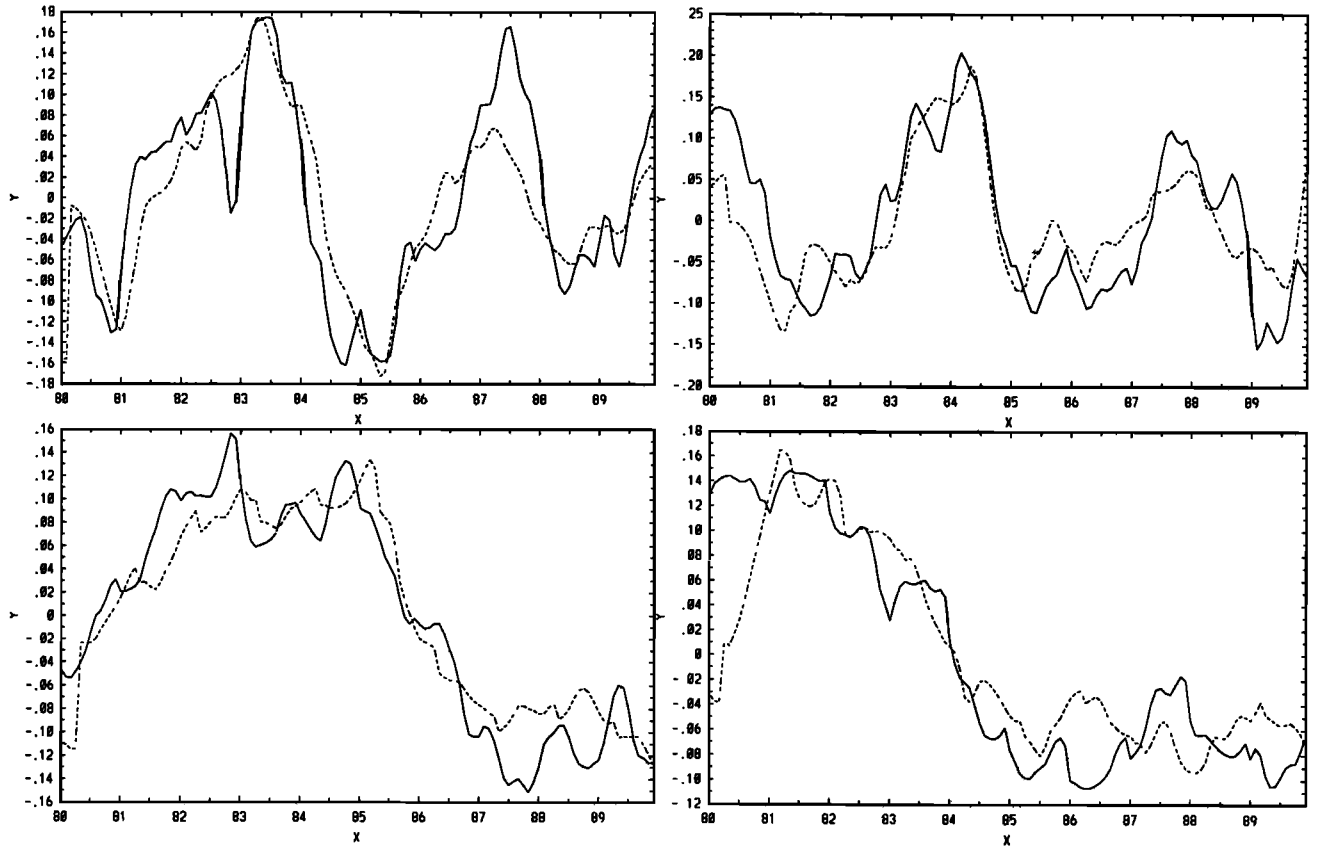

Figure 15. Evolution of the empirical time coefficients of the POPs of the simulated anomalies of heat content (solid line) and fit obtained through multivariated lagged regression from the PC of the integrated forcing fields. (Top left) The modeled time coefficient corresponding to the POP 2 of the anomalous heat content. The forcing field is the wind stress convergence; the optimal lag is -2 months. (Top right) The modeled time coefficient corresponding to the POP 1 of the anomalous heat content,ing The forcing field is the wind stress convergence; the optimal lag is -4 months. (Bottom left) The modeled time coefficient is of the POP 4 of the anomalous heat content, The forcing field is the wind stress divergence, the optimal lag is -1 months. (Bottom right) The modeled time coefficient correspond to the POP 3 of the anomalous heat content. The forcing field is the wind stress curl; the optimal lag is -3 months.

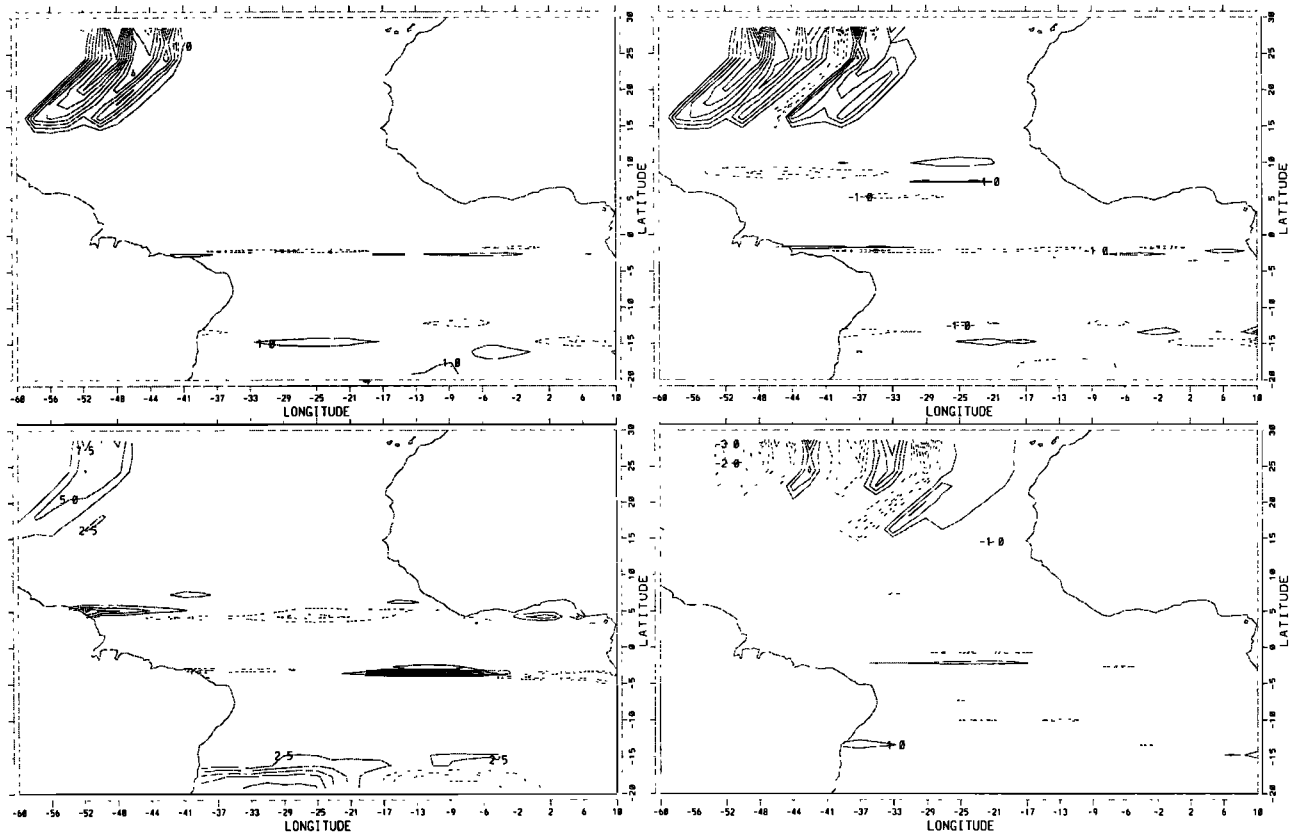

Figure 16. Patterns of the integrated forcing field associated by multivariated lagged regression (see (4), (5), and (6) in section 7) to the pair of POPs 2 (top left)/ 1(top right) and the pair of POPs 3 (bottom right)/ 4 (bottom left) of the anomalous heat content.

where $\vec{v}_j$ is the atmospheric pattern associated with the jth POP, $\vec{e}_k$ is the kth EOF, and a^l_{jk} are the coefficients determined in regression (6) at lag l.

In Figure 15 we present an example of the best fit of each of the POP time coefficients by the integrated fields, and in Figure 16 we present the corresponding associated patterns. POPs 1,2 and 3 of the heat content anomalies are connected through the multivariate regression (lags -6 to -1) to extraequatorial signals of the wind field stress in the northern hemisphere (north of 18°N). In the case of POP 1 the signal is centered in the Sargasso Sea, for POP 2 we have the same sort of signal reaching now the middle Atlantic and for POP 3, the signal is nearer the coast of Africa. The wavelike atmospheric activity at the equator, present in all these associated patterns, seems irrelevant compared with the importance of the extraequatorial signals.

8. Discussion

In the present work we try to simulate the equatorial Atlantic variability at annual and interannual timescales using an OGCM (OPYC) forced with observations for the period 1980-1989. To simulate an acceptable annual cycle, most of the Atlantic domain had to be included, and values at the boundaries are taken from an external source (what is called the open boundary condition). The performance of our model at simulating the variability at both timescales is comparable to that achieved by *Carton and Huang* [1994] and *Huang et al.* [1995] using a very different (Cox's) model forced by the same wind stresses, although the resolution of our model is much coarser. Except of the 1981 event, both models reproduce quite well the warming and coolings of the period, although they appear in the model earlier than in the observations. Furthemore, both overestimate the magnitude of the SST anomalies associated with the events. The failure of both models at reproducing the 1981 warming may be due either to a trend in the ECMWF wind stresses or to the unrealistic (climatological) initial state of the anomalous run.

As in the case of ENSO, the equatorial Atlantic warm events can be also understood as a redistribution of warm waters through the basin [*Wyrtki*, 1985]. The generation of the events is best monitored by a variable that captures the thermal structure of the ocean, like the heat content, which is able to give a full account of the generation of the events [*Chao and Philander*, 1993; *Latif and Graham*, 1992]. A statistical analysis of this field allows one to separate common traits from the peculiarities of each episode. Through an analysis in terms of principal oscillation patterns, the variability of the anomalous heat content field can be expressed in terms of only two pairs of patterns and their corresponding time coefficients. To explain the generation of the events, we try to relate the anomalies of heat content to those of the surface variables and to the forcings in a simple way. Only two of the four POP time coefficients that give the time evolution of the heat content anomalies can

be expressed in terms of the principal components of surface variables (SST, mixed layer depth, u and v mixed layer velocity). Those fits point to the convergence of the meridional mixed layer velocity as one of the important mechanisms that precedes the appearance of warm waters in the GG.

Due to the different timescales of variability, it is not possible to relate the anomalies of the heat content to those of the forcings using the simple multivariate lagged regression model. We define then some variables related to the forcings (wind stress divergence and curl), that measure their persistence at each point of the grid. The evolution in time of these new fields can be related to the heat contents through a linear model. The fitting of the POP time coefficients of heat content field by a combination of the six first principal components of either of the two new variables (the integrated wind stress divergence and its curl) is quite good. Through the regression coefficients, we determine four patterns of the forcing variables whose time evolution match those of the POP of the anomalous heat content. The patterns show important wavelike atmospheric activity at the equator. Persistent atmospheric anomalies in the northwest part of the basin are of relevance in three cases. The evolution of the fourth POP is connected to a signal north of 18°N, near the African coast.

There are a number of methods to relate output and forcing fields, as for instance, the extended empirical orthogonal function (hereinafter EEOF) analysis used by *Huang et al.* [1995]. The present procedure has three advantages compared with the EEOF procedure: (1) It gives a clearer picture of the evolution in time of the oceanic heat content anomalies. (2) Through the regression, we focused on the oceanic variability, which pertains to the analysis of a forced run. (3) The relationship between the fields can be compared with the EEOF procedure: (1) It gives a clearer picture of the evolution in time of the oceanic heat content anomalies. (2) Through the regression, we focused on the oceanic variability, which pertains to the analysis of a forced run. (3) The relationship between the fields can be checked through the tests of the quality of the fit. The significance of each pair of POPs is assessed through a partial reconstruction of the field using only this pair.

The picture of the generation of the events given by the first pair of POPs of the heat content anomalies agrees basically with *Wyrtki*'s [1985] hypothesis :"warm water accumulated in the west is displaced to the east". However, this mechanism is corrected by the second pair of POPs of this same field, to account for the differences in the generation of the the 1984 and the 1988 events. Concerning the relationships among the heat content and other oceanic variables or the forcing fields, the results presented above support and enlarge other results that have recently appeared and those obtained either from the HSC simulation or for a very simple statistical analysis of observations (difference between warm and cold years). For instance, *Carton and Huang* [1994] also find that the mass convergence in the meridional direction at the Gulf of Guinea is one of the mechanism that leads to the accumulation of warm waters there. The analysis of atmospheric observations by *Curtis and Hastenrath* [1995] points to the importance of some North Atlantic extraequatorial signals, similar to the ones presented in our associated patterns, for the weakening of the interhemispheric SST gradient and the subsequent warmings in the GG.

Appendix

A.1. Isopycnal Ocean Model

The basic quantities which should be conserved are momentum, energy, mass and potential vorticity. The basic equations are formulated in flux form as conservation equations for the vertical mean of the mass flux $(\rho\vec{v}h)_k$, the mass content $(\rho h)_k$, the heat content $(\theta\rho h)_k$ and the salt content $(S\rho h)_k$ in a column of the kth layer:

$$\begin{aligned}\frac{\partial}{\partial t}(\rho\vec{v}h)_k &= -\vec{\nabla}(\vec{v}_k(\rho\vec{v}h)_k) - h_k\vec{\nabla}p_k - \vec{f}\times(\rho\vec{v}h)_k \\ &+ \vec{\nabla}\cdot A_k^v\vec{\nabla}(\rho\vec{v}h)_k + (w\vec{\rho v})_k^{k+} + (w\vec{\rho v})_k^{k-} \\ &+ \vec{\tau}_k^{k-} + \vec{\tau}_k^{k+} - (w\vec{\rho v})_{k+}^{k} - (w\vec{\rho v})_{k-}^{k} \qquad \text{(A1)}\end{aligned}$$

$$\begin{aligned}\frac{\partial}{\partial t}(\rho h)_k &= -\vec{\nabla}\cdot(\rho\vec{v}h)_k + \vec{\nabla}\cdot A_k^h\vec{\nabla}(\rho h)_k \\ &+ R_k^h - (w\rho)_{k+}^{k} - (w\rho)_{k-}^{k} \\ &+ (w\rho)_k^{k+} + (w\rho)_k^{k-} \qquad \text{(A2)}\end{aligned}$$

$$\begin{aligned}\frac{\partial}{\partial t}(\theta\rho h)_k &= -\vec{\nabla}\cdot((\theta\rho h)\vec{v})_k + \vec{\nabla}\cdot A_k^s\vec{\nabla}(\theta\rho h)_k \\ &+ \frac{Q_k}{c_p} - (w\rho\theta)_{k-}^{k} - (w\rho\theta)_{k+}^{k} \\ &+ (w\rho\theta)_k^{k-} + (w\rho\theta)_k^{k+} \qquad \text{(A3)}\end{aligned}$$

$$\begin{aligned}\frac{\partial}{\partial t}(S\rho h)_k &= -\vec{\nabla}\cdot((S\rho h)\vec{v})_k + \vec{\nabla}\cdot A_k^s\vec{\nabla}(S\rho h)_k \\ &+ R_k^S - (w\rho S)_{k-}^{k} - (w\rho S)_{k+}^{k} \\ &+ (w\rho S)_k^{k-} + (w\rho S)_k^{k+} \qquad \text{(A4)}\end{aligned}$$

The terms $(w\vec{\rho v})$, $(w\rho)$, $(w\rho\theta)$, and $(w\rho S)$ describe exchange processes of mass fluxes, mass itself, heat, and salt content between neighboring layers. The different kinds of exchange processes are entrainment/detrainment and vertical exchange as cross-isopycnal mixing and convection. The terminology $(...)_k^l$ indicates a transfer from the kth layer into the kth layer, where l=k- represents the next upper and l=k+ the next lower (physically present) layer. N is the number of layers, the index k starting with k=1 in the uppermost layer (mixed layer). All terms in which 1- or N+ occur are set to zero, except for the term $\vec{\tau}_1^{1-}$ which represents the surface wind stress, and the term $\vec{\tau}_N^{N+}$ which represents the bottom stress. The term $\vec{\nabla}p_k$, the horizontal pressure gradient in a layer k, is computed as a sum of the sea level gradient, the gradients of the interface heights above the layer k and the potential density gradients integrated from the surface down into the center of layer k. The forcing function Q represents the heat flux, R^h the freshwater forcing, and R^S the forcing due to the sea ice - ocean coupling. Here c_p is the specific heat capacity of water, and f the Coriolis parameter. Since observed surface stresses are used, the surface drag coefficient does not need to be specified. The drag coefficients chosen for interfacial and bottom friction are different.

In order to complete the equations, in situ values of the density ρ, temperature T, salinity S and pressure P are related by the equation of state for seawater [*UNESCO*, 1981]. The in situ temperature T_k is calculated by inverting the formula of *Bryden* [1973], $\theta_k = \theta_k(T_k, S_k, P_k)$. By combining

the UNESCO formula for density with the formula for potential temperature, the potential density σ_θ can be defined by using the potential temperature and salinity in the same layer and reducing it to a specific reference pressure, chosen to be the sea surface pressure.

The diffusion coefficients, A^v_{ki}, A^v_{kj} and A^s_k depend on the grid spacing. This is useful if a grid with highly different resolution is chosen. By defining the damping timescales D_v ,$D_{v,1}$ for a vector quantity and T_s for a scalar quantity, the diffusion coefficient that is finally used automatically adjusts to the local numerical stability requirements at each grid point. In the present version of the model, the diffusion coefficient for vector quantities A^v_{kl} has different expressions for $l = i$ or $l = j$:

$$A^v_{ki} = \left(1+\frac{\Delta x^2}{a^2}\right)\left(1+\frac{\Delta x^2}{R_b^2}\right) D_{v,1} + \frac{(\Delta x^2)D_v}{(\Delta x^2+\Delta y^2)} \quad \text{(A5)}$$

$$A^v_{kj} = \left(1+\frac{\Delta y^2}{a^2}\right)\left(1+\frac{\Delta y^2}{R_b^2}\right) D_{v,1} + \frac{(\Delta y^2)D_v}{(\Delta x^2+\Delta y^2)} \quad \text{(A6)}$$

$$A^s_k = (\Delta x^2+\Delta y^2)/2T_s \quad \text{(A7)}$$

where $R_b = c/f$ is the Rossby deformation radius and $a = c/(2\beta)$ is the equatorial Kelvin wave deformation radius. Also, β stands for $\partial f/\partial y$ and the constant coefficients D_v and $D_{v,1}$ imply a dependence of the diffusion time on both the direction and the grid resolution. Δx and Δy are the grid distances in the converging spherical coordinates. The diffusion coefficient for vector quantities is split into two terms, the first varying latitudinally and the second depending on the grid resolution: At low latitudes both of them are equally important; at high latitudes the first one determines the diffusion. The Rossby deformation radius and that of Kelvin waves are taken as a measure to adjust the diffusion for each grid. The diffusion coefficient adjusts then automatically to refined resolution as well as latitude. This adjustment is intended to compensate for the smaller deformation radius, thus creating, for example, a Gulf Stream undercurrent .

A.2 Mixed Layer Model

A mixed layer (ML) is the result of turbulence produced by wind stirring and surface buoyancy fluxes. Temperature, salinity, and velocities are uniformly distributed in the vertical. The mixed layer height h is a prognostic variable, influenced not only by local mixing but also by horizontal convergence of mass or heat. Therefore the mixed layer model invokes the full dynamics of (A1) to (A4) combined with a parameterization for the vertical transfers of mass and related quantities across the mixed layer base. While entrainment enters the continuity equation (prognostic equation for the layer thickness) as a transfer rate between two adjacent layers, detrainment is treated diagnostically. The equation for the entrainment rate w is

$$wh[(1-\Gamma)g' + \Gamma g'_I] - wRi_{crit}(\Delta u^2+\Delta v^2) = 2m_o a u_*^3 + \Gamma h_I b B_I + (1-\Gamma)hbe(B-\gamma B_S) + (1-\Gamma)\gamma b B_S\left[h\left(1+\exp^{-h_I/h_B}\right) - 2h_B\left(1-\exp^{-h_I/h_B}\right)\right] \quad \text{(A8)}$$

where g' is the reduced gravity between the mixed layer and the next physical layer below and g'_I is the reduced gravity in the presence of sea ice [*Lemke*, 1987]. Ri_{crit} is the critical Richardson number, B is the total buoyancy flux through the surface that depends on the total heat flux Q, and on the corresponding equivalent heat flux due to the freshwater flux, $P-E$. B_s is the buoyancy flux due to the solar radiative heat flux Q_s. The entrainment/detrainment rate w is related to the transfer rates w^l_k in (A1) to (A4) by $w = w^{+1}_1$ if $w > 0$ and $w = w^l_{+1}$ if $w < 0$.

The first term on the left-hand side of (A8) describes the production of mean potential energy, and the second is the production of mean kinetic energy by entrainment. On the right-hand side, the first term stands for turbulent kinetic energy production due to wind stirring. The friction velocity is denoted by u_*. The free parameter m_o represents the effectivity of how turbulence available for mixing is produced by the mean wind stress. The following terms describe the influence of the surface buoyancy fluxes for the ice-covered and ice-free conditions, respectively. The last term, which is only nonzero for ice-free cases, represents the influence of penetrating solar radiation on the total buoyancy flux [*Denman and Miyake*, 1973].

The weighting coefficients a and b in (A8) are defined as exponential decay functions [see *Oberhuber*, 1993a]. Following *Paulson and Simpson* [1977], γ is the fraction of solar radiation that penetrates through the ocean surface and h_B is the depth at which the penetrating radiation has decayed to $1/e$.

In the retreat phase of the mixed layer the depth is determined by setting $w = 0$ in (A8) and solving for h, which gives the Monin-Obukhov length h_M. A second diagnostic calculation is carried out as soon as the flow becomes unstable due to excessive vertical shear. In this case a minimum depth h_{Ri} is defined through

$$h_{Ri} = Ri_{crit}(\Delta u^2+\Delta v^2)/g' \quad \text{(A9)}$$

As a result there are two constraints which limit the mixed layer depth. If the two constraints contradict each other, h_{Ri} is taken as criterion.

Acknowledgments. Thanks are due to J. Servain, who made his data sets available to us, and to the Laboratoire d' Océanographie Dynamique et Météorologie (LODYC) in Paris, wich supplied us with the FOQUAL-SEQUAL current measurements. The simulations reported in this paper were performed under contract EV5V-0124 and EV5V-CT94-0538C of the EU. Part of the computer time used was allotted at DKRZ(Hamburg) by the European Climate Computer Network (ECCN). When this time was exhausted, the Spanish Meteorological Office made additional CRAY hours available to us.

References

Arnault, S.A., Tropical Atlantic surface currents and ship drifts, *J. Geophys. Res., 92*, 5076-5088, 1987.

Carton, J. A. and B. Huang, Warm events in the tropical Atlantic, *J. Phys. Oceanogr., 24*, 888-903, 1994.

Chao, Y., and S.G.H. Philander, On the structure of the southern oscillation, *J. Clim., 6*, 450-469, 1993.

Curtis, S., and S. Hastenrath, Forcing of anomalous sea surface temperature evolution in the tropical Atlantic during Pacific warm events, *J. Geophys. Res., 100*, 15835-15847, 1995.

Denman, K. L., and M. Miyake, Upper layer modification at Ocean Station Papa: Observations and simulations, *J. Phys. Oceanogr., 3*, 185-196, 1973.

Duchene, C., and C. Frankignoul, Sensitivity and realism of wind driven ocean models, *J. Marine Syst., 1*, 97-117, 1990.

Gates W. L., AMIP: The Atmospheric Model Intercomparison Project, *Bull. Am. Meteorol. Soc., 73*, 1962-1970, 1992.

Hellerman,S., and M. Rosenstein, Normal monthly wind stresses over the world ocean with error estimates, *J. Phys. Oceanogr., 13*, 1093-1104, 1983.

Houghton, R. W., The relationship of sea surface temperature to thermocline depth at annual and interannual time scales in the tropical Atlantic Ocean, *J. Geophys. Res., 96*, 15173-15185, 1991.

Houghton, R. W., and Y. M. Tourre, Characteristics of low frequency sea surface temperature fluctuations in the tropical Atlantic, *J. Clim., 5*, 765-771, 1992.

Huang, B., J. A. Carton, and J. Shukla, A numerical simulation of the variability in the tropical Atlantic Ocean, *J. Phys. Oceanogr., 25* , 835-864, 1995.

Johns, W.E., T.N. Lee, F.A. Schott, R.J. Zantopp, and R.H. Evans, The North Brazil current retroflection: Seasonal structure and eddy variability, *J. Geophys. Res., 95*, 22103-22120, 1990.

Kauker F., and J.M. Oberhuber, An Isopycnal Ocean Circulation Model of the North Sea for Dynamical Downscaling *Rep. 97/E/47*, 29pp., GKSS Research Centre, Hamburg, 1997.

Latif, M., and T.P. Barnett, Interactions of the tropical oceans, *J. Clim., 8*, 952-964, 1995.

Latif, M., and N.E. Graham, How much predictive skill is contained in the thermal structure of an OGCM?, *J. Phys. Oceanogr., 22*, 951-962, 1992.

Lemke, P., A coupled one-dimensional sea-ice model, *J. Geophys. Res, 92*, 13164-13172, 1987.

Levitus, S., Climatological Atlas of the World Ocean, NOAA professional paper 13, U. S. Dept. of Commerce, 1982.

Miller, A. J., D.R. Cayan, T.P. Barnett,N.E. Graham, and J.M. Oberhuber, Interdecadal variability of the Pacific Ocean: Model response to observed heat fluxes and wind stress anomalies, *Clim. Dyn., 9*, 287-382, 1994.

Oberhuber, J. M., An atlas based on the COADS data set: The budgets of heat, buoyancy and turbulent kinetic energy at the surface of the global ocean, *Rep. 15*, 199 pp., Max-Planck-Inst. fuer Meteorol., Hamburg, 1988.

Oberhuber, J. M., Simulation of the Atlantic circulation with a coupled sea ice-mixed layer-isopycnal general circulation model, I, Model description, *J. Phys. Oceanogr., 23*, 808-829, 1993a.

Oberhuber, J. M., Simulation of the Atlantic circulation with a coupled sea ice-mixed layer-isopycnal general circulation model, II, Model experiment, *J. Phys. Oceanogr., 23*, 830-844, 1993b.

Paulson, C.A., and J.J. Simpson, Irradiance measurements in the upper ocean, *J. Phys. Oceanogr., 7*, 952-956, 1977.

Philander, S.G. H., and R. C. Pacanowski, A model of the seasonal cycle of the tropical Atlantic Ocean, *J. Geophys. Res., 91*, 14192-14206, 1986.

Richardson, P.L., and G. Reverdin, Seasonal cycle of velocity in the Atlantic North Equatorial countercurrent as measured by surface drifters, currentmeters and shipdrifts , *J. Geophys. Res., 92*, 3691-3708, 1987.

Schott, F.A., and C.W. Boening, The WOCE model in the western equatorial Atlantic : Upper layer circulation, *J. Geophys. Res., 96*, 6993-7004, 1991.

Servain, J., Simple climatic indices for the tropical Atlantic Ocean and some applications, *J. Geophys. Res., 96*, 15137-15146, 1991.

Servain, J., and D. M. Legler, Empirical orthogonal function analyses of tropical Atlantic sea surface temperature and wind stress: 1964-1979 applications, *J. Geophys. Res., 91*, 14181-14191, 1986.

Storch, H. von, G. Burger, R. Scnurr and J. S. Xu, Principal oscillation pattern analysis, *MPIM Rep. 113*,46 pp., Max-Planck-Inst. fuer Meteorol., Hamburg, 1993.

UNESCO, The practical salinity scale 1978 and the internal equation of the state of seawater 1980, *Tech. Pap. Mar. Sci., 36,pp.*, 13-21, Paris, 1981.

Weingartner, T. J., and R. H. Weisberger, On the annual cycle of equatorial upwelling in the central Atlantic Ocean,*J. Phys. Oceanogr., 21*, 68-82, 1987.

Weingartner, T. J. and R. H. Weisberger, A description of the annual cycle in sea surface temperature and upper ocean heat in the equatorial Atlantic, *J. Phys. Oceanogr., 21*, 83-96, 1991.

Wright, P., Variations in the tropical Atlantic sea surface temperature and their global relationships, *MPIM Rep. 12*, 52pp., Max-Planck-Inst. fuer Meteorol., Hamburg, 1987.

Wyrtki, K., Water displacements in the Pacific and the genesis of El Niño cycle, *J. Geophys. Res., 90*, 7129-7132, 1985.

W. CabosNarvaez and M. J. OrtizBeviá. Departamento de Física, Universidad de Alcalá, Apdo.20, 28880 Alcalá de Henares, Madrid, Spain. (e-mail: wl@ws3.fsc.alcala.es)

J. M. Oberhuber, Deustches Klimarechenzentrum, Bundestrasse 55, D-20146, Hamburg, Germany.

(Received February 17, 1997; revised September 10, 1997; accepted November 21, 1997)